https://doi.org/10.15407/ufm.24.03.561

A.V. ZAVDOVEEV[1,*], T. BAUDIN[2,], D.G. MOHAN[3,***], D.L. PAKULA[4,****], D.V. VEDEL[5], and M.A. SKORYK[4]**

[1] E.O. Paton Electric Welding Institute of the N.A.S. of Ukraine, 11, Kazimir Malevich Str., UA-03150 Kyiv, Ukraine

[2] Université Paris-Saclay, CNRS, Institut de Chimie Moléculaire et des Matériaux d'Orsay, F-91405 Orsay, France

[3] Department of Material Processing Engineering, Zhengzhou Research Institute of Harbin Institute of Technology, Zhengzhou, China

[4] G.V. Kurdyumov Institute for Metal Physics of the N.A.S. of Ukraine, 36, Academician Vernadsky Blvd., UA-03142 Kyiv, Ukraine

[5] I.M. Frantsevych Institute for Problems of Materials Science of the N.A.S. of Ukraine, 3, Omeljan Pritsak Str., UA-03142 Kyiv, Ukraine

* avzavdoveev@gmail.com, ** thierry.baudin@universite-paris-saclay.fr, *** dgmohan@hit.edu.cn, **** dpakula25@gmail.com

BASICS OF ADDITIVE MANUFACTURING PROCESSES FOR HIGH-ENTROPY ALLOYS

The review offers a comprehensive analysis of additive manufacturing (AM) processes in the application of high-entropy alloys (HEAs). HEAs have gained considerable attention in recent years due to their unique mechanical and physical properties. We provide the historical background and a clear definition of HEAs, outlining their development over time. The focus is concentrated on examining the utilization of AM processes in HEAs. Specifically, three prominent AM techniques are discussed: electron-beam processes, laser-processed HEAs, and wire-arc additive manufacturing. Each technique is explored in detail, including its advantages, restrictions, and current applications within the HEAs field. An attention is stressed on the significance of AM-process parameters during the fabrication of HEAs. Parame-

Citation: A.V. Zavdoveev, T. Baudin, D.G. Mohan, D.L. Pakula, D.V. Vedel, and M.A. Skoryk, Basics of Additive Manufacturing Processes for High-Entropy Alloys, *Progress in Physics of Metals*, **24**, No. 3: 561–592 (2023)

ters such as laser power, scanning speed, and powder-feed rate are analysed for their influences on the microstructure and mechanical properties of the final product. The post-processing techniques for additive-manufactured HEAs are considered. The importance of steps such as heat treatment, surface finishing, and machining in achieving the desired material properties and dimensional accuracy in AM-produced HEA components is underlined. Overviewing the HEAs, their application in AM processes, the influence of process parameters, and post-processing considerations, this work can act as a useful source of information for researchers on the way to amendment of the understanding and implementation of AM in the HEAs.

Keywords: additive manufacturing, high-entropy alloys, processing, structure, properties.

1. History and Definition of HEAs

Fascinating development of the alloy design brings us principally new materials with superior properties — high entropy alloys (HEAs). The history of creation is alloying principles, which firstly was based on one main element, or two, and other alloying elements in small amounts. A heightened presence of certain elements, for instance, Fe in Al alloys, can potentially result in a destructive impact [1]. However, the things were inversed drastically since 2004, when the multicomponent approach has given birth to HEAs. The authors of Refs. [2, 3] have proposed the new paradigm of alloy creation. This paradigm is based on the multicomponent main alloying system, normally more than 5 main elements. However, more recently, researchers have expanded the concept of HEAs to include alloys with three or four principal elements as well [4, 5] have presented a new approach to alloy design with multiple principal elements in equimolar or near-equimolar ratios. Despite general knowledge on physical metallurgy that predicted the formation of the multiple intermetallic compounds, when using multiprincipal elements, the real alloys appear much more usable and uniform. The configurational entropy changes per mole, based on Boltzmann's hypothesis, ΔS_{conf}, during the formation of a solid solution from n elements with equimolar fractions may be calculated as [2]:

$$\Delta S_{\text{conf}} = -k\ln(w) = -R(n^{-1}\ln(1/n) + n^{-1}\ln(1/n) + \ldots + n^{-1}\ln(1/n) = \\ = -R\ln(1/n) = R\ln(n). \quad (1)$$

Here, k is the Boltzmann's constant, w is the number of ways of mixing, and gas constant R = 8.314 J/(K·mole). Thus, ΔS_{conf} for equimolar alloys with 3, 5, 6, 9, and 13 elements equal to 1.10R, 1.61R, 1.79R, 2.20R, and 2.57R, respectively. In addition, if the formation enthalpies of two strong intermetallic compounds (*e.g.*, NiAl and TiAl) are divided by their respective melting points, the resulting ΔS_{conf}, 1.38R and 2.06R, belong to the same range as the entropy changes of mixing in a system with more than five elements [1]. This evidences that the tendency to

ordering is preferable when the high mixing entropy [6] suppresses the mechanism of segregation.

Thus, alloys with a higher number of principal elements will more preferably forms solid solutions during solidification, instead of intermetallic compounds, except for oxides, carbides, nitrides, and silicides with very large heats of formation.

According to Ref. [2], the high-entropy (HE) alloys are defined as those composed of five (starting from three according to updates) or more principal elements in equimolar ratios or HE alloys may contain principal elements with the concentration of each element being between 35 and 5 at.%. This has led to many alloy systems with simple crystal structures and extraordinary properties [7].

It is established that HEAs form different microstructures such as single-phase f.c.c., b.c.c., h.c.p. microstructures [8–10] as well as complex multi-phase microstructures [11]. These alloys have attracted great research interest owing to promising properties observed in specific HEAs. For instance, the quinary equimolar Cantor [3] HEA CrMnFeCoNi possesses an exceptional fracture toughness of more than 200 $MPa \cdot m^{1/2}$ at cryogenic temperatures, making it an ideal material for low-temperature applications [3]. As usual, HEAs are processed by powder metallurgy [12], conventional casting [8, 13] *etc.* To achieve the needed properties through refining the microstructures, the as-cast HEAs are processed by cold metal forming and/or annealing [8, 13]. The traditional metallurgical processes mentioned above are used to create simple geometry parts, with the requirement of post processing. Furthermore, there is a dilemma in the strength-plasticity relation for HEAs. Namely, some HEAs are very strong but restricted with plasticity (b.c.c. non-equiatomic $AlCoCrFeNiTi_{0.5}$ [14]), while there are very ductile but not strong enough (quinary equiatomic CrMnFeCoNi [15]). Cantor *et al.* [3] have reported [3] several HEAs with a five-component equiatomic HEA CrMnFeCoNi (Cantor alloy) and a series of six-, seven-, eight- and nine-component equiatomic HEAs. It is considered [3] a HEA consisting of 20 elements in equiatomic proportions, 5 at.% each of Mg, Sb, Si, Ge, Zn, Bi, Pb, Sn, Cd, Al, Nb, Mo, W, Ag, Cu, Ni, Co, Fe, Cr and Mn. However, HEAs are not restricted to equiatomic ratios. As mentioned above, Yeh *et al.* [2] expanded the scope of HEAs to alloys with multiple principal elements and concentration of each element between 5 and 35 at.%. There is appearance of non-equiatomic HEAs (*e.g.*, $Al_{0.5}CoCrCuFeNi$) [13] and four-component HEAs (*e.g.*, NbMoTaW) [16]. Some HEAs with trace elements have been also reported. For instance, Park *et al.* [17] investigated a novel Cantor alloy with 1 at.% C additions marked as 1%C–CrMnFeCoNi HEA. Therefore, in this point, HEAs reflect the alloys consisting of multiple elements, each in valuable atomic fractions (from 5 to 35 at.%), possibly with trace alloying elements. It should be

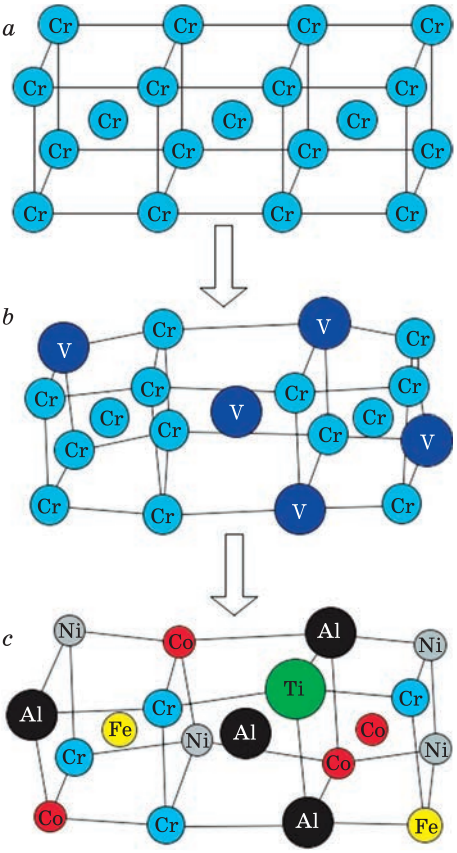

Fig. 1. Schematic illustration of severe lattice distortion of HEAs [20]: (*a*) b.c.c. crystal with a perfect lattice (*b*); distorted lattice due to the introduction of a element with different radius; (*c*) different elements with different (randomly distributed) radii

underlined that there are ternary equiatomic HEAs (*i.e.*, CrCoNi) in some literature named as medium entropy alloys (MEAs) [18, 19]. Unique compositional characteristics and large configurational entropy value of HEAs lead to severe lattice distortion (Fig. 1) due to the differences in atomic size, bonding energy, and crystal structure.

The HEAs as a rule exhibit a single-phase f.c.c., b.c.c., or h.c.p. solid solution microstructure. For instance, the quinary equiatomic Cantor HEA CrMnFeCoNi crystallizes as a single-phase f.c.c. solid solution structure [8, 21]. Moreover, a number of equiatomic quaternary (CrCoNiMn), ternaries (CrCoNi, FeNiMn, NiCoMn) also have a single-phase f.c.c. solid solution structure [5, 18, 22]. Quaternary non-equiatomic HEA $Fe_{40}Mn_{40}Co_{10}Cr_{10}$ exhibits a single-phase f.c.c. solid solution structure in as-cast, hot-rolled and homogenized states as reported by Deng *et al.* [23]. Such microstructure formation was observed in other HEAs (FeNiCrCuMo) [24]. The HEAs containing refractory b.c.c. metals such as W, Mo, Nb, Ta, and V typically crystallize as a single-phase b.c.c.-solid-solution structure in contrast to the f.c.c. HEAs. Namely, HEAs NbMoTaW and VNbMoTaW exhibit a single-phase b.c.c.-solid-solution structure as reported by Senkov *et al.* [16]. Single-phase b.c.c.-solid-solution microstructures were also registered for TaNbHfZrTi [25], MoNbHfZrTi [26], as well as for TaNbHfZr [27]. Notably that the metals Ti, Zr, and Hf have an h.c.p. structure at room temperature, changing to a b.c.c. structure at high temperatures revealing allotropic transformation. For a while, HEAs with a single-phase h.c.p. solid solution structure are rare and typically contain several h.c.p. metals such as Y, Ru, Re, Gd, Tb, Dy, Tm, *etc.* (YGdTbDyLu, GdTbDyTmLu, and CoFeReRu) [9, 28].

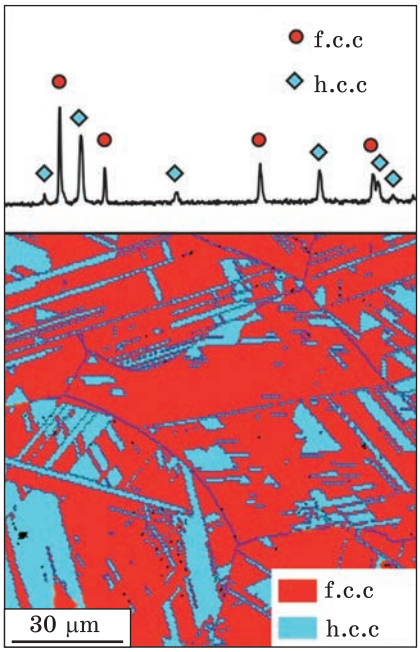

Fig. 2. XRD profile and EBSD phase map of $Fe_{50}Mn_{30}Co_{10}Cr_{10}$ HEA [29]

Additionally, to single-phase f.c.c.-, b.c.c.- or h.c.p.-solid-solution microstructures, multiphase microstructures consisting of multiple solid solution phases were also registered in some HEAs. Li *et al.* [29] have shown that the quaternary non-equiatomic HEA $Fe_{50}Mn_{30}Co_{10}Cr_{10}$ acquires a dual-phase f.c.c.- plus h.c.p.-solid-solution microstructure due to partial martensitic transformation after quenching from the single-phase f.c.c. region. Figure 2 shows the as-quenched microstructure that consists of a 72% f.c.c. matrix with ≈45-

Phases and alloying systems of some typical HEAs

Crystal structure	Alloy system	References
f.c.c.	CrCoNiMn CoNiFeMn CrCoNiFe CrCoNiFePd CrMnFeCoNi FeNiCrCuCo FeNiCrCuMo $Fe_{40}Mn_{40}Co_{10}Cr_{10}$ $FeCoCrNiC_{0.05}$ $Fe_{50}Mn_{30}Co_{10}Cr_{10}$	[5, 18, 21, 23, 24, 29]
b.c.c.	$AlCoCrFeNiMo_x$ NbMoTaW NbMoTaW VNbMoTaW MoNbHfZrTi TaNbHfZrTi TaNbHfZr $AlCoCrFeNiMo_x$	[16, 25, 27, 30]
h.c.p.	YGdTbDyLu GdTbDyTmLu CoFeReRu	[9, 28]

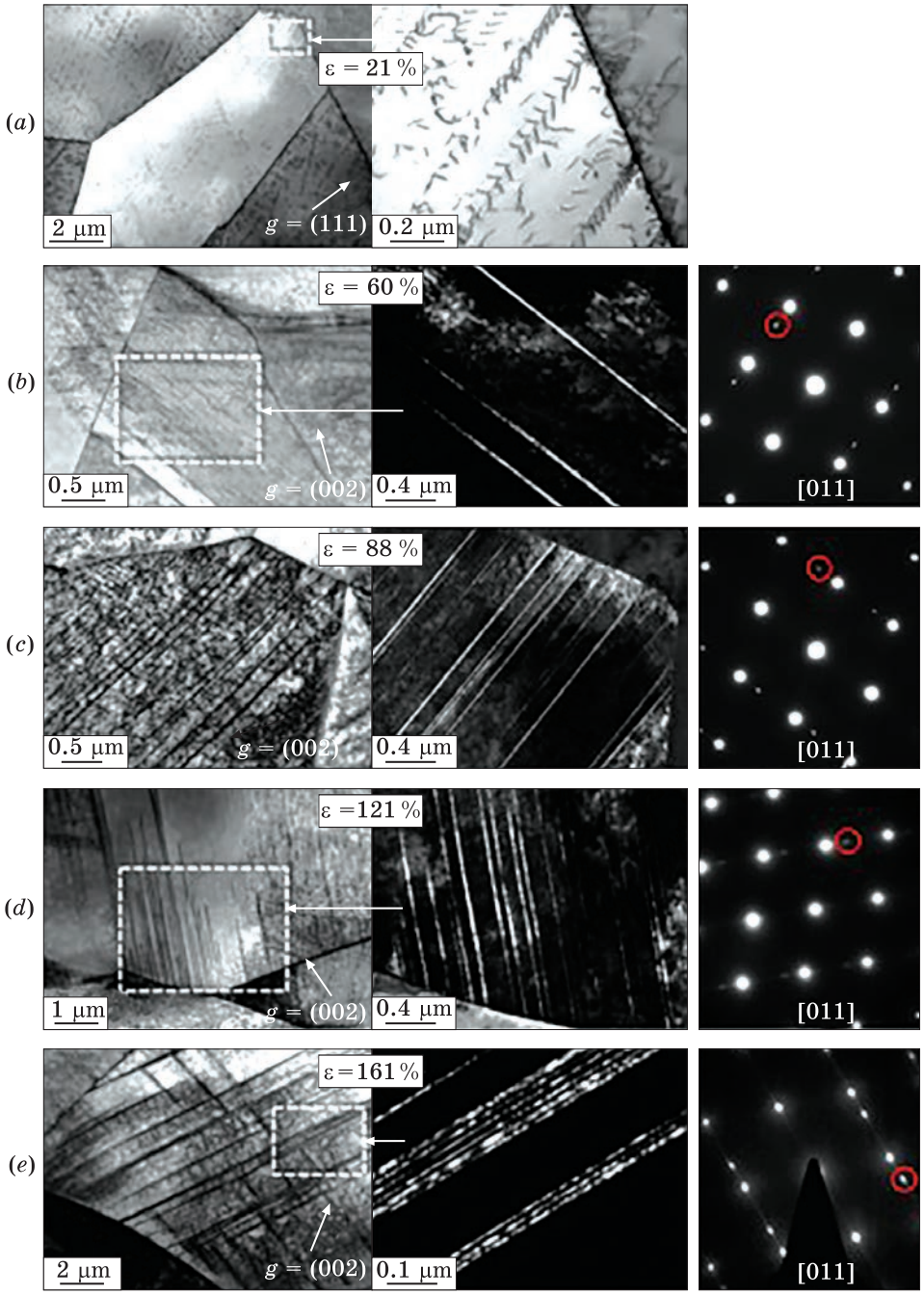

Fig. 3. The formation and hence evolution of the deformation substructures during tensile straining of CrMnFeCoNi at 77 K [31]

μm grain size plus 28% h.c.p. layers from several nanometers to 10 μm in thickness. The typical HEAs are presented in Table.

There are complex deformation mechanisms in HEAs: dislocation motion, nanotwinning, or martensitic phase transformation. Concerning these deformation mechanisms, f.c.c. Cantor HEA CrMnFeCoNi [21, 31] was the most investigated. For example, the formation and evolution of the deformation substructures in CrMnFeCoNi during tensile straining have been studied [31]. The tensile deformation process is dominated by dislocation motion at low strain levels. With further strain levels increasing up to ≈7.4% for 77 K and ≈25% for 293 K, nanotwinning is activated and plays an additional deformation mechanism. The strain hardening capability is increased through the nanotwinning behaviour that introduces more interfaces. Figure 3 shows the formation and hence evolution of the deformation substructures in CrMnFeCoNi during tensile straining at 77 K. Instead of the tensile test while compression, a larger strain value may be needed to activate the nanotwinning mode, since mechanical twinning is still minor when CrMnFeCoNi is compressed to 46% strain [32].

High-entropy alloys are manufactured through a range of techniques, which are chosen based on the desired properties, alloy composition, and specific application needs. The prevailing fabrication methods for HEAs include casting, powder metallurgy, and additive manufacturing. Casting, although effective, requires substantial energy consumption and necessitates the use of a furnace with an inert atmosphere [33, 34]. Powder metallurgy, while viable, is labour-intensive [35]. Consequently, additive manufacturing emerges as an appealing alternative due to its potential for optimizing the trade-off between fabrication time and energy consumption in the context of HEAs.

2. AM Processes in the HEAs Application

The AM process produces samples, layer by layer, from a digital design, which increases design and manufacturing freedom. Complex elements can be fabricated in a single step by the AM process, requiring little or no post-machining. The AM process is a localized melting and solidification process that has high solidification velocity and a significant temperature gradient. Moreover, it is possible to achieve hierarchical microstructures characterized by the presence of fine grains, solidification patterns, and dislocation substructures through the fabrication process contributing to exceptional mechanical properties [36]. Additionally, *in situ* phase decomposition during the AM process can lead to the formation of the desirable microstructures and hence good mechanical properties [37, 38]. These advantages are the most important argument for the increasing interest in the fabrication of HEAs through

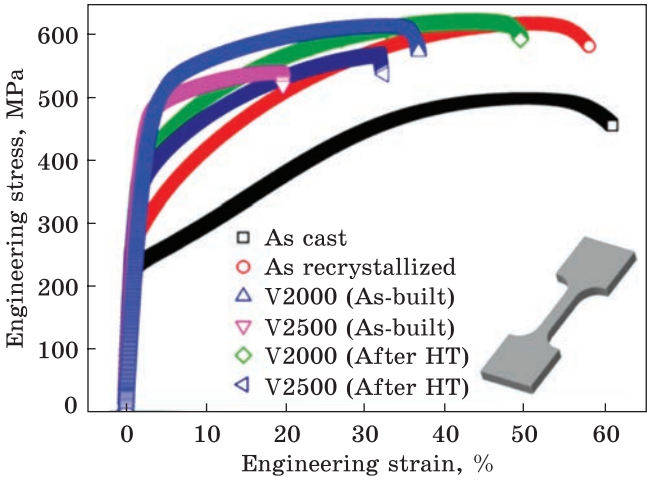

Fig. 4. The engineering stress–strain curves of the CrMnFeCoNi with different conditions, where V2000 and 2500 indicate the velocity in mm/s [41]

the AM process. There are a number of HEAs processed by various AM processes with different processing parameters: $Al_xCoCrFeNi$ [22, 39], $Co_{1.5}CrFeNi_{1.5}Ti_{0.5}Mo_{0.1}$ [40], CrMnFeCoNi [41, 42], TiZrNbMoV [9], C-containing CrCoNiFe [43] and compositionally graded HEAs, *i.e.*, $AlCo_xCr_{1-x}FeNi$ ($0 \le x \le 1$) [44].

The rapid heating, melting followed by rapid resolidification of materials in the scale of the melt pool with subsequent numerous reheating–recooling cycles of the as-solidified region, are characteristic for AM process [45]. This complex thermal process determines the solidified microstructures, phase formation, grain structure and substructure, defects, cracks and pores formation, and thus the mechanical properties. Therefore, investigating this thermal process, mostly the rapid solidification process, is of valuable importance for the AM process.

The first such work was done by Brif *et al.* in 2015 [22], where they adopted a numerical approach based on the Rosenthal model, to reveal a relationship between the melt penetration depth and a number of printing parameters for selective laser melting (SLM). The printing parameters, to ensure that the layers can be fully melted, were identified, and the FeCoNiCr HEA with high strength and ductility were successfully fabricated. In another work, Sun *et al.* [46] have found that the FeCoNiCr HEA is addicted to solidification cracking under the SLM process, and predicted that the decreased grain size can effectively decrease the depression pressure and thus suppress the solidification cracking susceptibility. The equilibrium and non-equilibrium solidification processes were simulated [47] with the aim to predict the phase formation and elemental redistribution of HEAs. From the elemental powder blends using the laser metal deposition (LMD) process, CrMnFeCoNi HEA was successfully printed. CrMnFeCoNi HEA with hierarchical microstruc-

tures was also additively manufactured by Zhu *et al.* [21] with mechanical properties comparable to as-casted counterparts (Fig. 4).

It should be emphasized that the tensile properties of the additively manufactured HEA CrMnFeCoNi were reported to vary in a wide range for yield strength: 200–600 MPa and uniform elongation: 20–60% [48, 49]. This evidences that different manufacturing parameters lead to varied microstructures, namely grain size. These arguments show that the micrometallurgy of AM process plays a key role in HEAs application.

Thus, the strength–plasticity point of the AM HEAs is still a great problem to be solved. For example, CrMnFeCoNi obtained with AM is the most investigated HEA up to now. It has been manufactured successfully with a good combination of strength and ductility that compares to those as-casted counterparts [41, 49]. Some refractory HEAs with high-strength and low-plasticity have been also fabricated, Moorehead *et al.* [50] (Mo–Nb–Ta–W, single-phase disordered b.c.c. structures), Dobbelstein *et al.* [51] ($Ti_{25}Zr_{50}Nb_0Ta_{25}$ to $Ti_{25}Zr_0Nb_{50}Ta_{25}$), Kunce *et al.* [52] (ZrTiVCrFeNi and TiZrNbMoV). Additionally, the AlCoFeNiSmTiVZr HEA system has been also produced by the SLM process, with the research focused on the corrosion features [53].

For different applications, HEAs, owing to large compositional design space, offer unique possibilities to construct mechanical and functional properties of materials. The base effects of high configurational entropy, lattice distortion, mixing effect, and slow diffusion lead to a spectre of attractive physical-mechanical, properties [19, 54, 55]. HEAs can be considered as potential materials for advanced applications such as nuclear, aerospace, cryogenics, *etc.* [56, 57]. Due to specific restrictions, it is challenging task to fabricate of HEAs with homogeneous microstructure in complex geometries using traditional approaches. Therefore, AM has been of growing interest in HEAs application.

2.1. Electron Beam Processes

Fabrication of HEAs using selective electron-beam melting (SEBM) have been published in several reports [58, 59]. Successful fabrication of the equiatomic AlCoCrFeNi HEA using SEBM was reported by Fujieda *et al.* [40, 58], Kuwabara *et al.* [59], and Shiratori *et al.* [60]. For SEBM-built HEA, nanolamellar morphology with a mixture of f.c.c. + b.c.c. + *B*2 phases was registered caused by preheating, while as-cast counterpart showed only a b.c.c. + *B*2 structure. At the bottom of the sample, f.c.c. density was higher and as formed mostly at grain boundaries possibly due to longer preheating, which leads to phase transformation from the b.c.c. phase to f.c.c. one. The amount of *B*2 was also higher in the bottom part of the sample. In the top part of the SEBM sample, the columnar grain with the orientation of ⟨100⟩ along build direction was observed

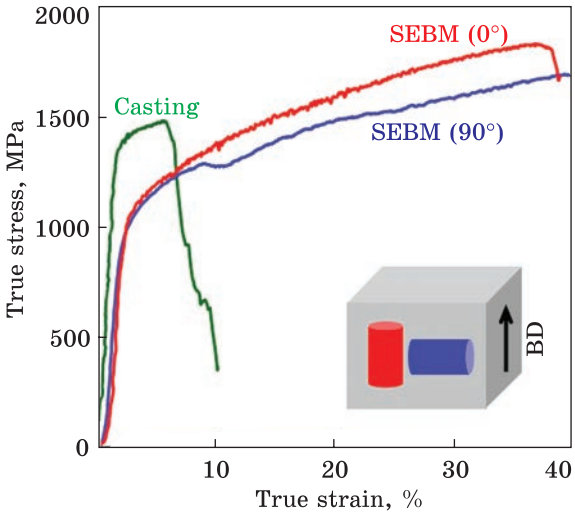

Fig. 5. True stress–strain plot of AlCoCrFeNi HEA fabricated using the selective electron beam melting (SEBM) and compared with as-cast sample [58]

and, in the bottom, equiaxed grains with random orientation were formed. The smaller grain size of the SEBM process in comparison with as-casted is explained by a higher cooling rate. Moreover, only in the SEBM sample, due to specific cooling conditions, the cellular microstructure was observed. The elemental distribution of both the SEBM and as-cast alloys reveal fluctuation inside the grains, and the segregation of Co and Fe at the grain boundaries as well as at subgrain boundaries. A similar microstructure was obtained for CoCrFeMnNi HEA produced using EBM [61]. The hierarchical microstructure with large columnar grains along build direction (strong ⟨100⟩ texture) and cellular dendritic structure for EBM built CoCrFeMnNi HEA was reported by Wang *et al.* [61]. The equiaxed grains perpendicular to the build direction with intragranular cellular dendritic microstructures were observed. The segregation of Fe, Cr, and Co into the dendrites, and Mn and Ni segregated into the interdendritic regions were found. The needle-like Ni_3Ti intermetallics in $Co_{1.5}CrFeNi_{1.5}Ti_{0.5}Mo_{0.1}$ HEA fabricated using EBM were revealed during microstructure characterization. Phases with basket-weave morphology precipitated homogeneously in the matrix, and were dissolved during solution treatment with a nanosize single-cubic-ordering phase was precipitated caused by spinodal decomposition [40]. The SEBM manufacture of $Al_{0.5}CrMoNbTa_{0.5}$ HEA using a blend of elemental powders can be possible through the optimization of the process parameters as shown in Ref. [18].

The mechanical properties of the EBM-fabricated CoCrFeNiMn HEA parts displayed similar tensile properties as in as-casted condition and were studied by Wang *et al.* [61]. The predominant deformation mechanism was dislocation with the less contribution of twinning.

The EBM-fabricated AlCoCrFeNi HEA showed relatively lower strength and ductility than in as-cast conditions (Fig. 5) [58]. The fracture strength is six times higher than a conventional engineering material SUS304 and equal to 1400 MPa for EBM samples. In addition, such properties were observed for samples whose cylinder axes were parallel

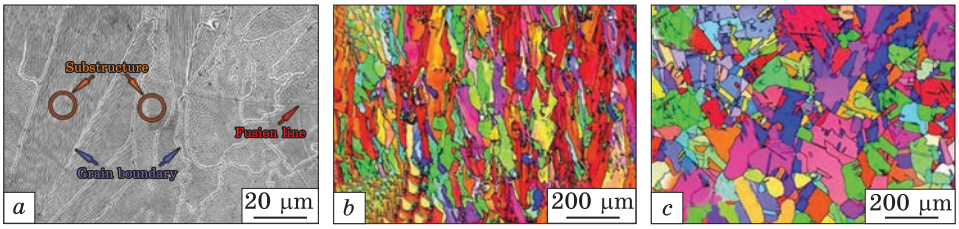

Fig. 6. (*a*) Images from scanning electron microscope (SEM) for SLM-built CoCrFeNi HEA showing its cellular structure. Electron back-scattered diffraction (EBSD) of CoCrFeNi HEA for (*b*) as built and (*c*) annealed conditions, confirming columnar microstructure for as-built and equiaxed for annealed sample [64]

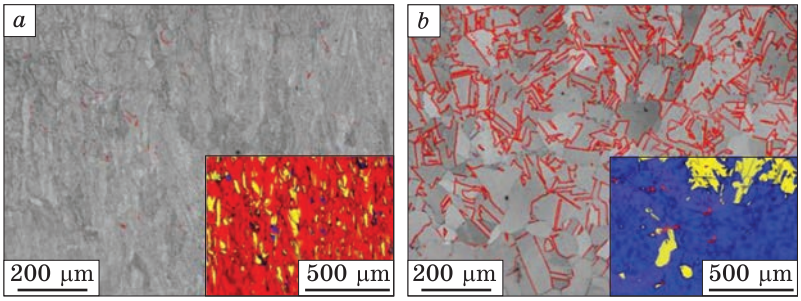

Fig. 7. Distribution of twinning for CoCrFeNi HEA for (*a*) as-built and (*b*) annealed at 1300 °C for 2 h conditions, indicating higher density of twinning after annealing. Insets show recrystallization distribution pattern [64]

and perpendicular to the build direction and, which approve its anisotropic behaviour [58]. Moreover, the higher tensile strength and ductility in heat-treated EBM-fabricated $Co_{1.5}CrFeNi_{1.5}Ti_{0.5}Mo_{0.1}$ HEA is superior to the as-cast sample found by Fujieda *et al.* [40].

2.2. Laser Beam Processes

As was shown in Ref. [62], SLM-fabricated AlCoCrFeNi HEA reveals a dual-phase structure with epitaxial growth of columnar disordered b.c.c. phases and ordered b.c.c. phases (*B*2) precipitation. The increase in volumetric energy density (VED) caused an increase in the *B*2-phase fraction [62]. The chemical composition of the powder has a critical effect on the morphology and quality of the final product as well. For example, with an increase in Ni content, the microstructure of $AlCrCuFeNi_x$ HEA SLM manufactured is changed from columnar to equiaxed grains structure [63]. The SLM-fabricated $AlCrCuFeNi_{3.0}$ HEA reveal heterogeneous microstructures consisting of nanosize lamellar dual-phase f.c.c. and *B*2 structures, twins, and the coherently precipitated b.c.c. nanophase

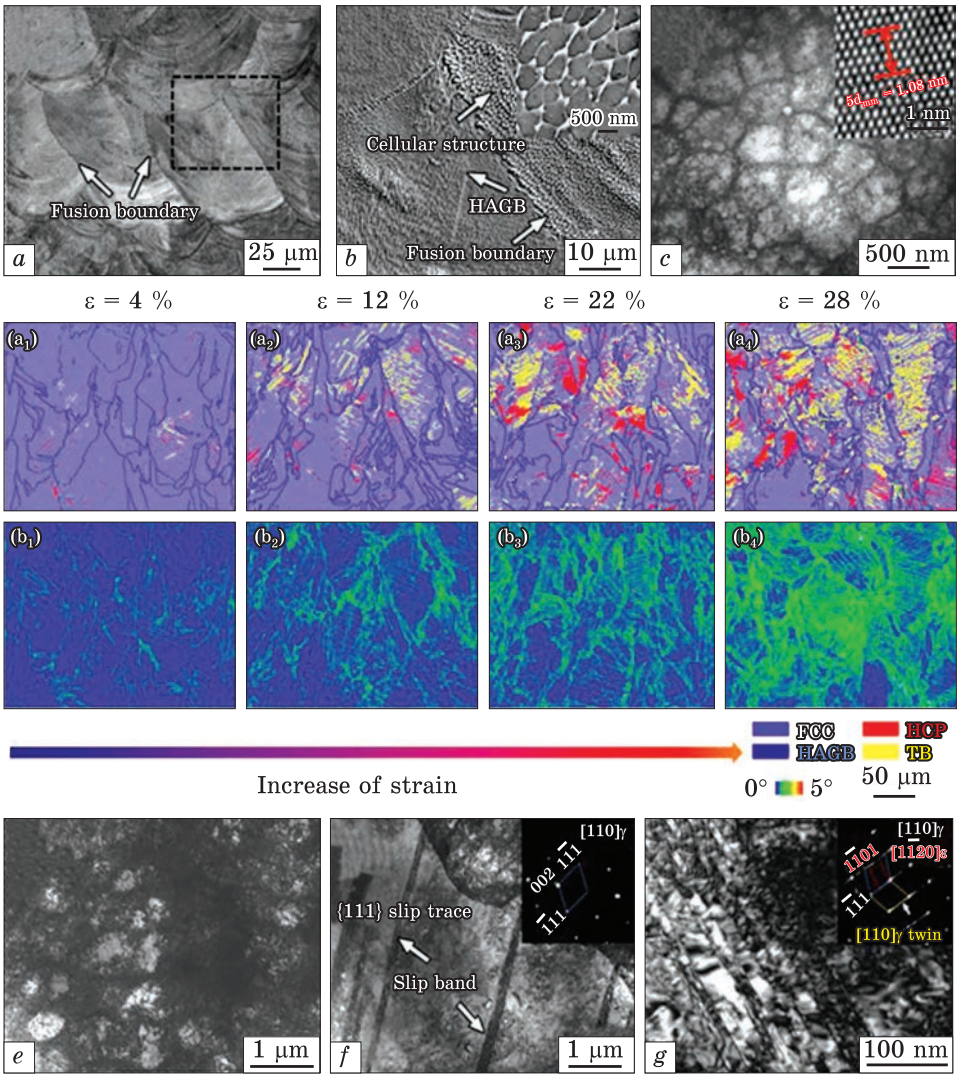

Fig. 8. (*a*) Optical microscope (OM) images of the as-built $Fe_{49.5}Mn_{30}Co_{10}Cr_{10}C_{0.5}$ HEA. (b) Scanning electron (SE) image of dotted region in (*a*). The inset displays the equiaxed cellular structures. (*c*) Scanning TEM (STEM) micrograph showing the equiaxed cellular structures. The inset shows the distance across five {111} planes in high-resolution transmission electron microscopy (HRTEM) image. (*d*) EBSD phase and grain boundary (GBs) maps revealing microstructural evolution at different strain levels (a_1–a_4). Transmission electron microscopy (TEM) images of deformed structure for 4% (*e*, *f*) and 12% strain (*g*). The insets show the selected area electron diffraction (SAED) pattern [70]

within the *B*2 phase [63]. The SLM-printed CoCrFeNi HEA studied by Lin *et al.* [64] possesses columnar grain microstructure with cellular structures and a large number of dislocations at grain boundaries (Fig. 6, *a*, *b*). Heat treatment at 1300 °C for 2 h caused to the formation of equiaxed grains (Fig. 6, *c*), and twins (Fig. 7, *a*, *b*).

The most common CoCrFeMnNi Cantor HEA is used for powder-based additive manufacturing. It showed f.c.c. crystal structure as in as-cast condition and SLM as well [65]. There are different results concerning the microstructure of SLM-fabricated CoCrFeMnNi, *i.e.*, the columnar microstructure of the alloy along the build direction [48] or the mixed morphology of columnar and equiaxed grains [66] are reported. Further, the authors have used laser-based AM at laser power in the range of 600–1000 W manufacturing of equiatomic CoCrFeMnNi HEAs [66]. There has been found that higher laser power led to a decrease in porosity and then an increase in density of the sample. The fabricated alloy showed mixed columnar and equiaxed grain microstructure [66]. The columnar grain size changed from 2 to 7 μm with an increase in laser power from 600 W to 1000 W. A similar microstructure was observed in Chew *et al.* [49] research. After annealing at 1100 °C, the microstructure became to recrystallized grain structure [66]. The cellular structure was also registered in several works [67, 68]. In these researches, the SLM-built CoCrFeMnNi HEA possesses a uniform composition and cellular subgrains with the grain boundary angle less than 5°, whereas, the as-cast sample has coarse dendrite crystals. The dislocation pile-ups, nanotwins, lattice distortion, and Mn segregation at the boundaries of the melt pool in the microstructure characterization of SLM CoCrFeMnNi is reported by Li *et al.* [65].

To develop an additional strain hardening mechanism in HEAs through introducing interstitial atoms, such as carbon, boron, *etc.* has attracted great attention [69, 70]. The carbon simultaneously activated twinning-induced plasticity (TWIP) and transformation-induced plasticity (TRIP) mechanisms in metastable $Fe_{49.5}Mn_{30}Co_{10}Cr_{10}C_{0.5}$ HEA as was reported in Ref. [71]. The possibility of fabricating interstitial carbon strengthened HEA using SLM process was studied in Ref. [70]. The $Fe_{49.5}Mn_{30}Co_{10}Cr_{10}C_{0.5}$ HEA with hierarchical microstructure (Fig. 8, *a*–*c*) was successfully fabricated by SLM. The yield strength (≈710 MPa), tensile strength (1000 MPa) and elongation at failure (28%) of the manufactured sample were much higher than those of coarse grain as-casted one [71]. The deformed samples microstructure showed planar slip bands, deformation twins, and phase transformation at the early stage of straining (Fig. 8, *d*–*f*). At further straining, the intersected stacking faults (SFs) and slip bands were registered (Fig. 8, *g*)). These multiple deformation peculiarities were stated to be favourable for work-hardening behaviour and lead to notable strength–ductility enhancement.

3. Wire Arc Additive Manufacturing

Firstly, the wire arc additive manufacturing (WAAM) is conditioned by the cost-effectiveness. The heating source in such a scheme is an electric arc. For filler material, welding wire is used. The combination of these two factors gives valuable benefit and gain before high-energy laser or electron beam tools. Direct energy deposition attracts more and more attention in additive manufacturing design research. Considering gas metal arc welding (GMAW) as the most widespread, it should be taken into account the operating mode. This means special welding current, voltage, welding speed, *etc.*

As shown in Ref. [72], the gas tungsten arc (GTA) WAAM with pre-alloyed wire can be a suitable alternative manufacturing route for the Al0.1CoCrFeNi HEA with predetermined composition. The microstructure characterization, and mechanical testing results have proved the efficiency of WAAM for HEAs. The results obtained by the authors have shown that the energy density is identified as the primary factor governing the bead continuity, and an energy density higher than 80 J/mm^3 is required to deposit a uniform bead. For good energy density, a range of heat input conditions could be suitable with different travel speeds of welding.

The high heat input results in a faster build speed and improved material efficiency, surface quality compared to the low heat input. An extremely high heat input leads to a wide bead with a low profile. This will require more layers to be deposited to reach a determined height. The molten metal may drip at a certain deposit height is reached. It has been shown that low as well as high heat input deposits have similar yield strength (260 MPa), ultimate tensile strength (420 MPa), and ductility (45–55%), comparable to as-casted metal. The high heat input deposit has a 10% higher ductility and lower hardness than the low heat input one. This is caused by the structure formation, *i.e.*, grain size increase. Consequently, the low heat input deposit has a slightly higher hardness due to a higher dislocation density as well. The optimal process parameters for GTA–WAAM of $Al_{0.1}$CoCrFeNi high-entropy alloy have been determined as follows: 200 A (current), 2000 mm/min (wire feed speed), and 200 mm/min (travel speed). The mechanical property evaluation in this study as well as fractography is presented in Fig. 9.

Another one approach in WAAM is based on a combined cord with several types of wires and reported by [73]. For the first time, a new type of combined cable wire (CCW) with multielement composition has been designed and developed for the WAAM of non-equiatomic Al–Co–Cr–Fe–Ni high-entropy alloy [73]. These CCW are composed of 7 filaments and 5 chemical elements. As shown by the authors, this approach has the advantages of high deposition efficiency, self-rotation of the welding arc, and energy-saving capability (Fig. 10).

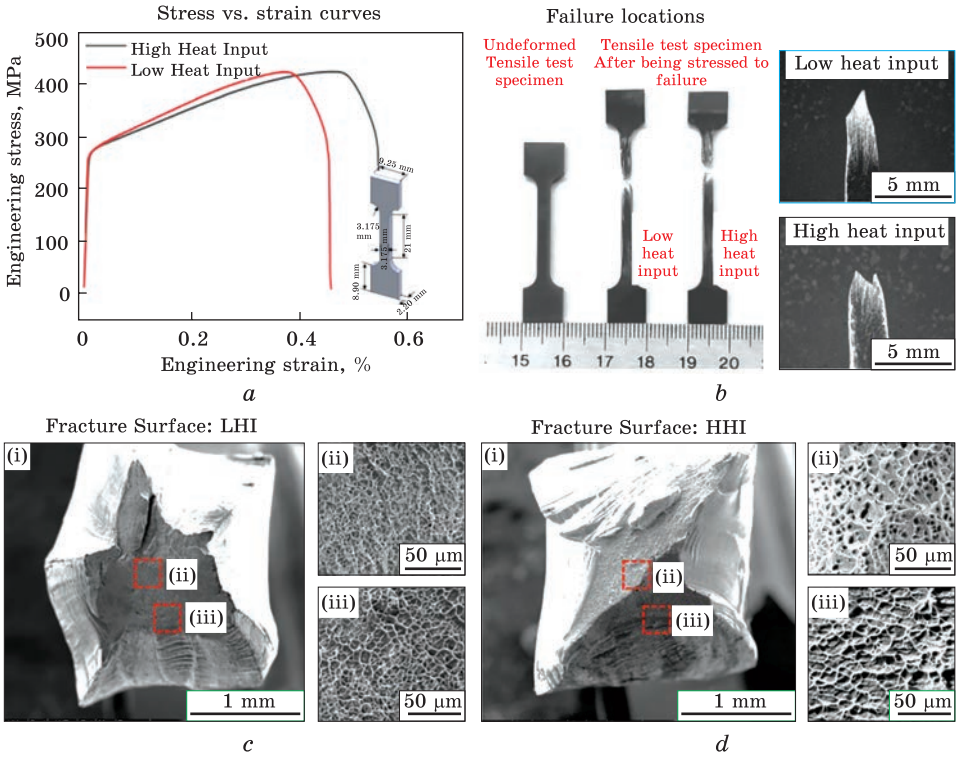

Fig. 9. (*a*) Stress *vs.* strain curves for the tensile testing of the deposits with two heat input conditions. (*b*) OM images showing the failure locations. SEM images of the fracture surfaces of the (*c*) low heat input and (*d*) high heat input specimens [72]

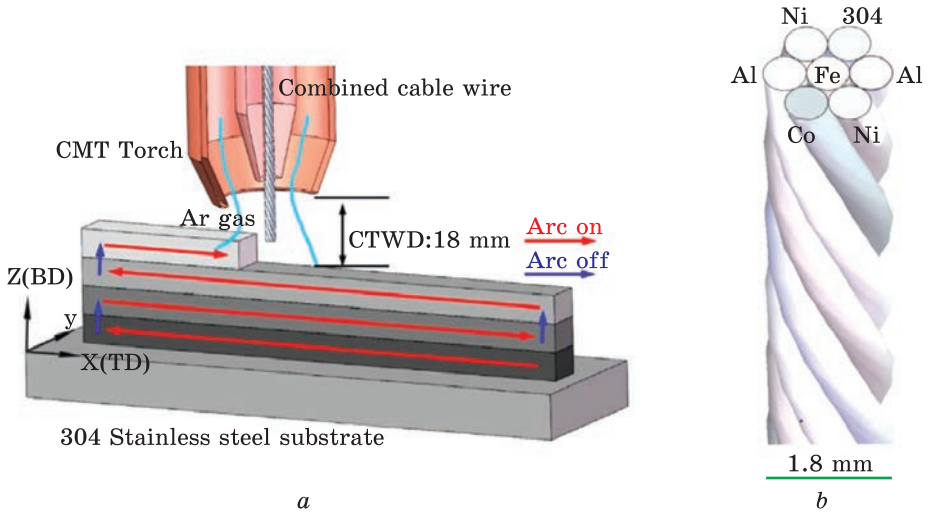

Fig. 10. (*a*) Schematic of the CCW-AAM (combined cable wire arc additive manufacturing) technique used to create HEA and (*b*) 3*D* model of CCW [73]

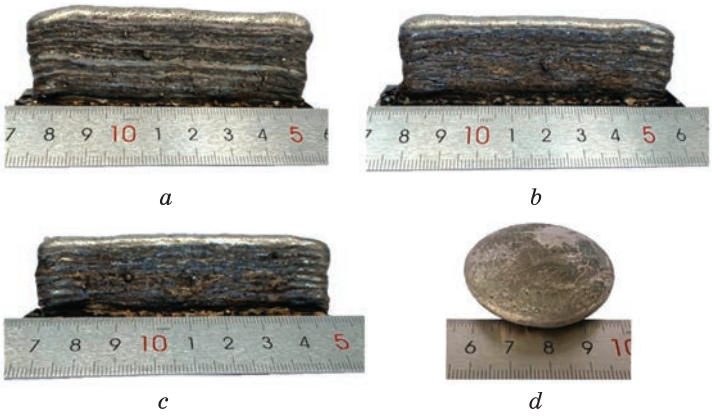

Fig. 11. Samples of Al–Co–Cr–Fe–Ni HEA fabricated using CCW-AAM: (*a*) 8 mm/s travel speed; (*b*) 10 mm/s travel speed; (*c*) 12 mm/s travel speed; (*d*) vacuum arc casting [73]

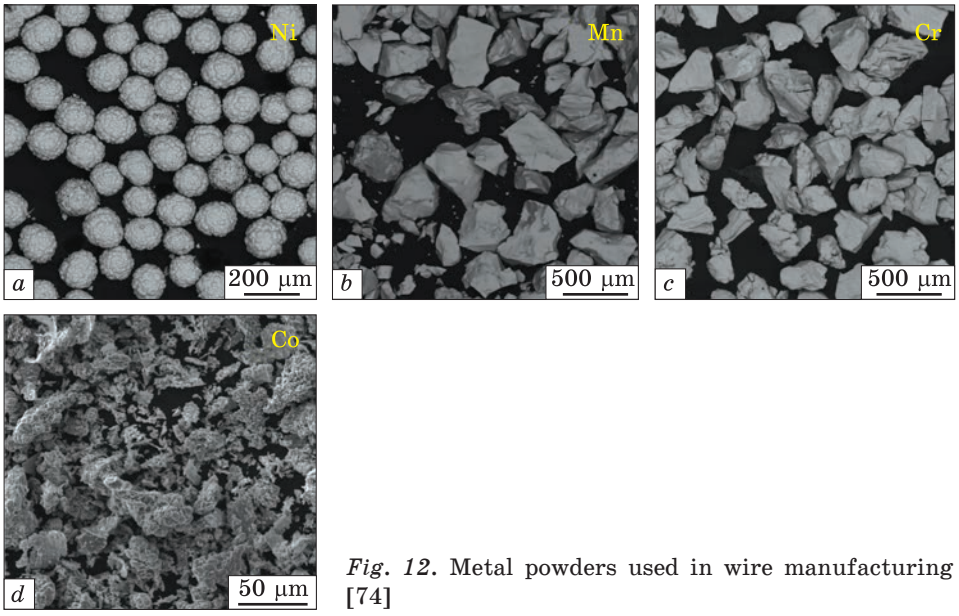

Fig. 12. Metal powders used in wire manufacturing [74]

The thin HEA walls were manufactured under pure argon gas using cold metal transfer technology. The microstructural characterization has revealed b.c.c. and f.c.c. phases, good bonding between layers, and defect-free microstructure (Fig. 11). The fabricated Al–Co–Cr–Fe–Ni alloy exhibits high compression strength of 2900 MPa with high elongation ≈42% values, and then, possesses both very good strength and ductility. It has been shown [73] that by varying the heat input, the

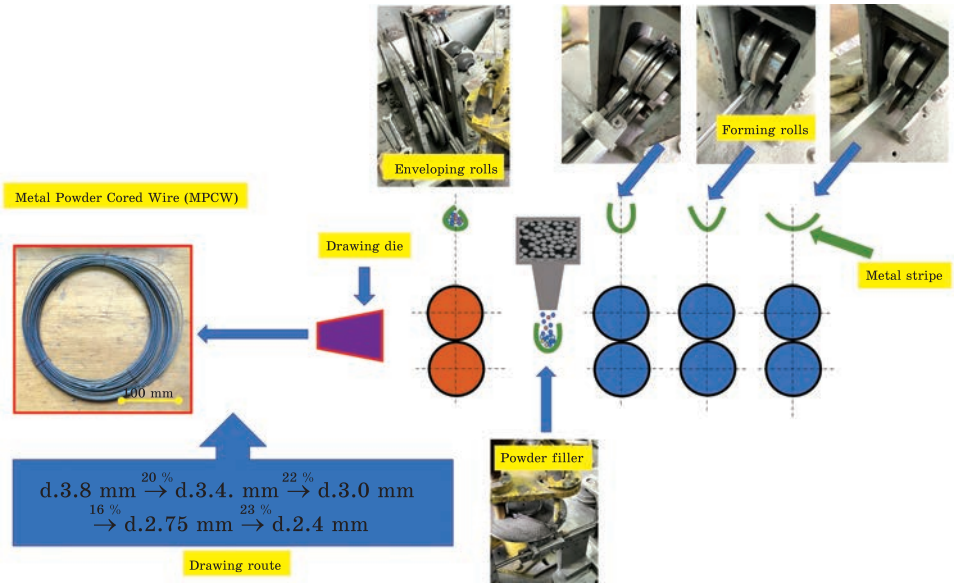

Fig. 13. Scheme of the metal powder cored wire manufacturing

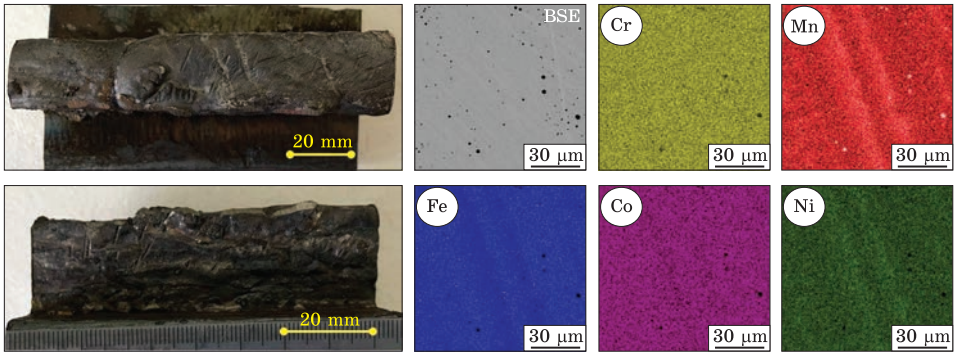

Fig. 14. A general view of deposits and x-ray maps of the chemical elements distribution

microstructure and mechanical properties of this alloy can be controlled. It has been proved that the innovative CCW can be successfully used in the WAAM of the HEAs.

Thus, combination of DED GMAW with combination with welding wire opens perspectives for pushing forward the development of the HEA manufacturing. The metal powder-cored wire (MPCW) is beneficial in comparison with solid wire [72] due to difficulties of the production of last. Either drawing of the solid wire or combining several thin wires in one cord [73].

For the production of the MPCW with a diameter d = 2.4 mm, an ultralow carbon steel stripe with a size of 0.4×10 mm^2 was used, the filling coefficient was of 60%, and the wire construction was single-layer [74].

The introduction of cobalt, manganese, chromium, and nickel powders in the amount of 20–25% each (Fig. 12) into the steel stripe tube provides high entropy composition of the whole wire. The filling coefficient is about 60%, and its ratio to the wire diameter is within 25 units. At a ratio of more than 27 units in the shell of the wire, there are microcracks that contribute to the destruction of the metal powder cored wire, which leads to the impossibility of its use for welding.

The manufacturing procedure scheme and creation route are presented in Fig. 13. The manufacturing route includes several stages, first is the formation U-shape form of the metal stripe, which is realized with the help of the forming rolls. The second is the filling of the U-shape metal stripe with metal powder mixture using a special tool, namely a funnel with a disc. The third stage is the enveloping U-shape metal stripe into O-shape one with the help of the drawing die. Moreover, the final stage is the drawing procedure aimed to get the needed wire diameter. Here, there are peculiarities of the drawing process, which consists of the partial reduction during drawing is not exceed 23% [75]. Hence, the MPCW wire drawing route was selected as follows: d = 3.8 mm $\rightarrow$ d = 3.4 mm $\rightarrow$ d = 3.0 mm $\rightarrow$ d = 2.75 mm $\rightarrow$ d = 2.4 mm (the partial reduction 20% $\rightarrow$ 22% $\rightarrow$ 16% $\rightarrow$ 23%, respectively).

The VDU-506 power supply is used for metal deposition, the welding parameters were as follows, welding current 280–350 A, arc voltage 32–34 V, temperature between welds 200–250 °C. The additive manufacturing of the high-entropy alloy using metal powder cored wire with the GMAW process is proposed. Welding is performed in modes that provided stable combustion of the arc, which is achieved at a wire feed speed of 77–90 mm/s.

The developed MPCW, an additively manufactured three-dimensional sample of the high-entropy alloy of the Cantor doping system is grown. In total, ten layers of deposition will be performed, which made it possible to obtain a monolithic sample measuring $150 \times 35 \times 20$ mm^3 (Fig. 14).

4. AM Process Parameters

The most valuable point of AM is the possibility to control the final product through a bottom-up approach where the microstructure and properties of the fabricated product can be controlled through the process by intellectually choosing the process parameters [54]. As the material is being built locally by melting and solidification, the cooling rate and melt pool size can be varied by controlling process parameters such

as source power, speed, *etc.* [54]. The final microstructure of the products is a function of additional parameters such as build atmosphere, build orientation, scanning strategy, and spacing between two adjacent lines that beam traces, in case of the beam melting. Researchers are choosing parameters such as power, scanning speed, lines spacing, and quantifying them into a common variable: 'volumetric energy density (VED)', 'laser energy density' and sometimes the 'linear laser energy density' [76, 77] in case of the laser AM. Additionally to the process parameters, the powder feedstock quality has also a significant effect on the quality of the manufactured product. Powder qualities are analysed based on their composition, purity, and microstructure as well as particle morphology, density, size distribution, and flow ability [78].

The AM process is controlled by a combination of several process parameters such as powder quality, deposition pattern, laser power and laser scan speed in the case of SLM process. The gas atomized (GA) powders is be more favourable to be hollow [79]. The stored gas in the GA particles may not escape out of the melt pool while the AM process, due to high cooling rates, and can lead to the increased porosity of the fabricated product. The deposition scheme has a significant effect on the resulting residual stress as well. As reported by Nickel *et al.* [80], a raster deposition scheme with the scan vector rotated by 90° between layers produces a smaller residual stress and thus a lower deflection. Concerning the final grain structure, the substrate orientation is affected [81].

In connection that HEAs have metastable nature, their AM is challenging, and the as-built samples usually have defects such as crack, pores, *etc.*, as mentioned above. A number of parameters like powder composition and AM parameters need to be optimized to obtain HEA samples free of any defects. Research on the effect of VED on quality parts of AM HEAs showed that low VED increased the probability of delamination between the successive layers, cracking, and porosity. Balling can occur if insufficient VED or high scanning speed [82]. An optimal level of VED at relatively slow scan speed improved layer-by-layer bonding and densification as well as the molten pool flow ability. Instead, high VED resulted in the keyhole porosity and scattering of molten metals [83]. Thus, an optimized range of VED is needed to manufacture HEAs defect-free product [69].

5. Post-Processing of the Additive Manufactured HEAs

Despite the above-mentioned AM process parameters, the post-treatments have been proven effective for improving the mechanical properties of the AM products [79, 84]. The annealing heat treatment leads to the increased ductility of SLM-manufactured Al–12Si alloy [85], despite

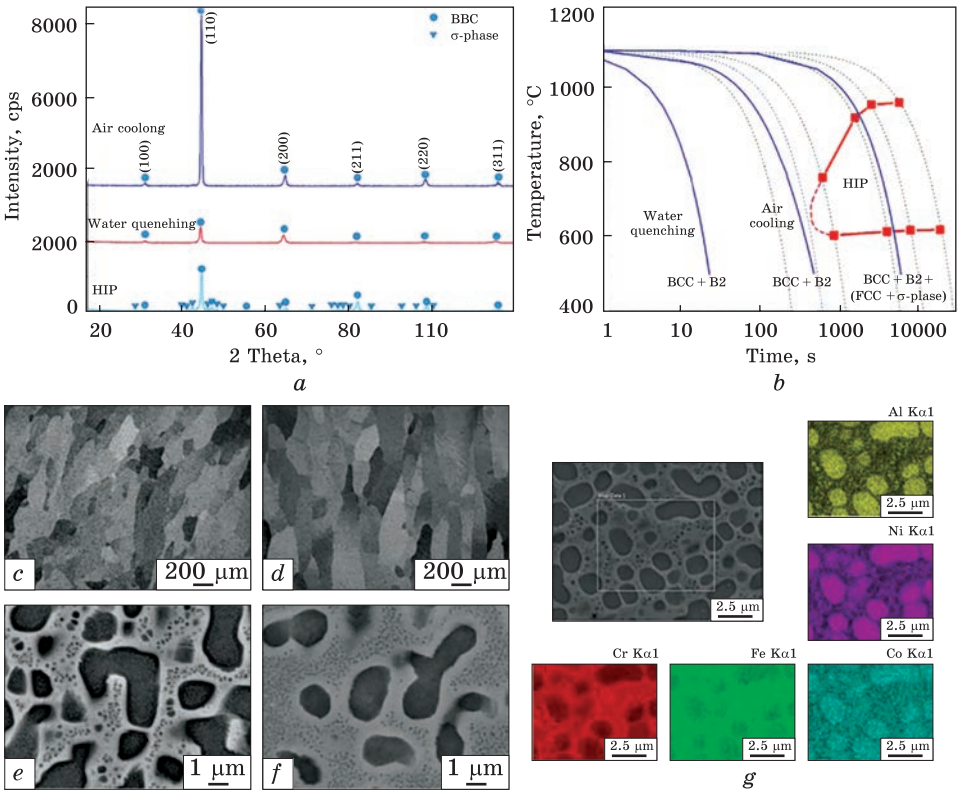

Fig. 15. (*a*) The XRD spectra of $Al_{0.85}CoCrFeNi$ HEA subjected to various post-processing heat treatments after solutionising at 1100 °C for 3 h with cooling rates of air-cooling water quenching and HIP (*b*) shown on the continuous cooling transformation (CCT) curve of σ-phase in $Al_{0.85}CoCrFeNi$ alloy. SEM micrographs of $Al_{0.85}CoCrFeNi$ alloy solutionised at 1100 °C for 3 h followed by (*c*) air cooling and (*d*) water quenching and the corresponding micrographs at higher magnification (*e*–*g*), respectively [92]

decreasing strength, and an improved strength–ductility relation is reached. The ultrasonic post-processing leads to increasing the bending strength and bending modulus of AM alloys as reported by Wu *et al.* [86]. Thus, the post-treatment and process parameters are required to be determined carefully.

The post-processing treatments of the additively manufactured HEAs such as cold deformation [87], thermomechanical processing [88], annealing [89], homogenizing [90], and aging [91], impact a positive influence on the microstructure and thus mechanical properties. In addition, the hot isostatic pressing (HIP) [92] is an elevated temperature densification process that is also an effective tool for structure enhancement (Fig. 15) and, thus, properties. It has been widely used in additive

manufactured metallic components to heal defects such as hot cracking, voids [93], as well as to homogenize the microstructure [94]. The high isostatic pressure reduces the size and density of porosity, without changing the shape of the manufactured parts, due to high temperature softens the alloy, as well known.

The exploration of the deformation and annealing behaviours of high-entropy alloys with a ductile high-entropy alloy of $Al_{0.5}CoCrCuFeNi$ are reported in Ref. [89]. As shown by the authors, $Al_{0.5}CoCrCuFeNi$ had excellent workability and exhibited a large work hardening capacity in both hot forging and cold rolling. It has been shown that the main deformation and hardening mechanisms are associated with the nanotwinning deformation during cold work. Namely, the blockage by the Widmanstätten Cu-rich precipitates of local slip deformation in a space of several tens of nm results in easy formation of nanotwins, as well as low stacking fault energy. Also, it was shown that $Al_{0.5}CoCrCuFeNi$ have higher resistances to static anneal softening than traditional alloys with comparable melting points during annealed in 5 h at 900 °C. This resistance is attributable [89] to extensive solution hardening, low stacking fault energy, and the effect of sluggish diffusion.

The microstructure and electrochemical corrosion behaviour of the $FeCoNiCrCu_{0.5}$ HEAs annealed at various temperatures were studied in Ref. [95]. The effects of annealing temperatures of 350, 650, 950, and 1250 °C with a holding time of 24 h at each temperature on the alloy microstructure and properties were shown. The x-ray diffraction (XRD) spectra of the initial sample and heat-treated to 1250 °C showed an f.c.c.-solid-solution phase. This HEA contained a matrix, with a Cu-depleted phase, a Cr-rich phase (second structure), and a Cu-rich phase (third structure). Authors have found that the Cr-rich phase precipitated in the matrix after annealing at 1250 °C and spinodal decomposition of the Cu-rich in the annealing temperature from 350 to 1250 °C. The electrochemical corrosion behaviours of the as-cast and annealed specimens have shown that it was severely corroded in 3.5% NaCl solution caused by precipitation of the Cu-rich phase in the matrix. The Cl-ions preferentially attacked Cu-rich phase, which is attributed to the fact that the presence of copper in the alloy degraded the corrosion resistance by pitting.

The microstructure and mechanical properties of $Al_xCoCrFeNi$ HEAs were systematically studied in Ref. [90]. The post-processing treatment of homogenization and deformation has been applied for HEAs with varied Al content. It has been shown that single f.c.c. and single b.c.c. solutions, and duplex f.c.c.–b.c.c. are principal phases in these alloys. The spinodal decomposition of Al–Ni phases is the major reaction during the homogenization of the $Al_xCoCrFeNi$ HEAs was considered. It has been shown that there is no stress-induced phase transformation

during 50%-rolling deformation, and the main strengthening mechanism is work hardening and the hardening ability of f.c.c. was about twice that of b.c.c. in this alloy system [90].

In other work [87], the f.c.c.-$Al_{0.3}$CoCrFeNi HEA was nanostructured by post-processing treatment with high-pressure torsion (HPT). It was revealed that the HPT of this alloy exhibits a higher hardness increment than most single-phase materials, a combination of HPT and annealing significantly strengthens the HEA hardness owing to the formation of a secondary ordered b.c.c. phase, and after HPT and annealing is ≈ 4 times highest hardness over for the as-cast HEA.

To transform the coarse dendritic structure to the cast AlCuCrFeNiCo HEA, the extensive multistep forging at 950 °C was applied [88] to form a fine equiaxed duplex structure consisting of the mixture of b.c.c. and f.c.c. phases. They have shown that hot forging post-processing treatment of the HEA made it stronger and more ductile during testing at room temperature than the as-cast alloy. Namely, the yield stress, ultimate tensile strength, and tensile ductility of the post-processed metal were 1040 MPa, 1170 MPa, and 1%, respectively, against 790 MPa, 790 MPa, and 0.2% for the as-cast condition. In the as-cast condition, brittle to ductile transition occurred between 700 and 800 °C, while in the forged condition, it was observed between 600 and 700 °C. Authors have found [88] that in the temperature range of 800–1000 °C, the post-processed alloy showed superplastic behaviour with elongation above 400% and even reached 860% at 1000 °C.

The microstructure evolution in CoCrFeNiMn HEA during uniaxial compression to a height reduction corresponding to the true strain of ≈1.4 in the temperature interval 600–1100 °C was studied in Ref. [96]. The differences in the mechanical behaviour of the alloy and the activation energy of deformation below and above 800 °C temperature intervals were observed. It has been shown that microstructure evolution at studied temperatures was found to be accompanied by discontinuous dynamic recrystallization (DDRX). The DRX was primarily associated with the nucleation of new grains on the initial grain boundaries, during hot deformation, when in the warm interval, DDRX was mainly observed in shear bands. In this case, the volume fraction of the recrystallized structure was 0.085 at 600 °C and 0.95 at 1000 °C, with the grain sizes of 0.2 and 40.4 μm, respectively.

6. Summary and Conclusions

The high-entropy alloys exhibit a range of advantages, making them highly appealing in various applications [97–100]. Additive manufacturing techniques have emerged as a promising approach for fabricating HEAs, offering distinct advantages over conventional methods. Addi-

tionally, AM software provides the capability to simulate printing processes, including the melting pool and AM techniques, allowing for improved process optimization. While this review does not delve into the specifics of such simulations, they hold potential for enhancing future research endeavours.

Comparisons of AM process parameters, particularly volumetric energy density, among different techniques enable a deeper understanding of their effects on HEA fabrication. This knowledge aids in selecting the most suitable AM technique for specific applications and optimizing the resulting material properties.

Regarding post-processing after AM, considerations such as the necessity of hot isostatic pressing or the sufficiency of simple annealing depend on the desired material characteristics and application requirements. These factors should be carefully evaluated to achieve the desired performance of the final HEA product.

Looking ahead, promising prospects include the exploration of novel HEAs with unique compositions and properties, as well as the investigation of underutilized AM techniques for HEA fabrication. Additionally, identifying new applications that can leverage the exceptional attributes of HEAs in additive manufacturing holds significant potential for advancing the field.

We believe that this review work highlights the advantages of HEAs, the benefits of AM techniques over conventional methods, the potential of AM software for simulation, the importance of process parameters, the significance of post-processing considerations, and the prospects for future advancements in HEA research and applications.

REFERENCES

1. P. Ashtari, K. Tetley-Gerard, and K. Sadayappan, Removal of iron from recycled aluminium alloys, *Can. Metall. Q.*, **51**: 75–80 (2012).
2. J.-W. Yeh, S.-K. Chen, S.-J. Lin, J.-Y. Gan, T.-S. Chin, T.-T. Shun, C.-H. Tsau, and S.-Y. Chang, Nanostructured high-entropy alloys with multiple principal elements: novel alloy design concepts and outcomes, *Adv. Eng. Mater.*, **6**: 299–303 (2004).
https://doi.org/10.1002/adem.200300567
3. B. Cantor, I.T.H. Chang, P. Knight, and A.J.B. Vincent, Microstructural development in equiatomic multicomponent alloys, *Mater. Sci. Eng. A*, **375–377**: 213–218 (2004);
https://doi.org/10.1016/j.msea.2003.10.257
4. S. Chen, Y. Tong, and P.K. Liaw, Additive manufacturing of high-entropy alloys: a review, *Entropy*, **20**: 937 (2018).
5. Z. Wu, H. Bei, G.M. Pharr, and E.P. George, Temperature dependence of the mechanical properties of equiatomic solid solution alloys with face-centered cubic crystal structures, *Acta Mater.*, **81**: 428–441 (2014);
https://doi.org/10.1016/j.actamat.2014.08.026

6. E. Johnson, Cohesion in metals: (Cohesion and structure, vol. 1) by F.R. de Boer, R. Boom, W.C.M. Mattens, A.R. Miedema and A.K. Niessen (Elsevier, Amsterdam, 1988) pp. xiv + 758, hardbound, US $ 131.50/Dfl 250-. ISBN 0-444-87098-9, *Nuclear Instruments and Methods in Physics Research Section B: Beam Interactions with Materials and Atoms*, **42**, No. 3: 403 (1989); https://doi.org/10.1016/0168-583X(89)90456-4
7. K. Wu, N. Ding, T. Yin, M. Zeng, and Z. Liang, Effects of single and double pulses on microstructure and mechanical properties of weld joints during high-power double-wire GMAW, *J. Manuf. Process.*, **35**: 728–734 (2018); https://doi.org/10.1016/j.jmapro.2018.08.025
8. B. Gludovatz, A. Hohenwarter, D. Catoor, E.H. Chang, E.P. George, and R.O. Ritchie, A fracture-resistant high-entropy alloy for cryogenic applications, *Science*, **345**, No. 6201: 1153–1158 (2014); https://doi.org/10.1126/science.1254581
9. A. Takeuchi, K. Amiya, T. Wada, K. Yubuta, and W. Zhang, High-entropy alloys with a hexagonal close-packed structure designed by equi-atomic alloy strategy and binary phase diagrams, *JOM*, **66**: 1984–1992 (2014); https://doi.org/10.1007/s11837-014-1085-x
10. C.L. Tracy, S. Park, D.R. Rittman, S.J. Zinkle, H. Bei, M. Lang, R.C. Ewing, and W.L. Mao, High pressure synthesis of a hexagonal close-packed phase of the high-entropy alloy CrMnFeCoNi, *Nat. Commun.*, **8**: 15634 (2017); https://doi.org/10.1038/ncomms15634
11. Y.-J. Liang, L. Wang, Y. Wen, B. Cheng, Q. Wu, T. Cao, Q. Xiao, Y. Xue, G. Sha, Y. Wang, Y. Ren, X. Li, L. Wang, F. Wang, and H. Cai, High-content ductile coherent nanoprecipitates achieve ultrastrong high-entropy alloys, *Nat. Commun.*, **9**: 4063 (2018); https://doi.org/10.1038/s41467-018-06600-8
12. W. Ji, W. Wang, H. Wang, J. Zhang, Y. Wang, F. Zhang, and Z. Fu, *Intermetallics*, **56**: 24–27 (2015); https://doi.org/10.1016/j.intermet.2014.08.008
13. Z. Tang, T. Yuan, C.-W. Tsai, J.-W. Yeh, C.D. Lundin, and P.K. Liaw, Fatigue behavior of a wrought $Al_{0.5}$CoCrCuFeNi two-phase high-entropy alloy, *Acta Mater.*, **99**: 247–258 (2015); https://doi.org/10.1016/j.actamat.2015.07.004
14. Y. Zhou, Y. Zhang, X. Wang, Y. Wang, and G. Chen, Effect of component substitution on the microstructure and mechanical properties of *M*CoCrFeNiTi$_x$ (*M* = Cu, Al) solid-solution alloys, *Rare Met.*, **27**: 627–631 (2008); https://doi.org/10.1016/S1001-0521(08)60195-3
15. W.H. Liu, Y. Wu, J.Y. He, T.G. Nieh, and Z.P. Lu, Grain growth and the Hall–Petch relationship in a high-entropy FeCrNiCoMn alloy, *Scr. Mater.*, **68**: 526–529 (2013); https://doi.org/10.1016/j.scriptamat.2012.12.002
16. O.N. Senkov, G.B. Wilks, J.M. Scott, and D.B. Miracle, Mechanical properties of $Nb_{25}Mo_{25}Ta_{25}W_{25}$ and $V_{20}Nb_{20}Mo_{20}Ta_{20}W_{20}$ refractory high entropy alloys, *Intermetallics.*, **19**: 698–706 (2011); https://doi.org/10.1016/j.intermet.2011.01.004
17. J.M. Park, J. Choe, J.G. Kim, J.W. Bae, J. Moon, S. Yang, K.T. Kim, J.-H. Yu, and H.S. Kim, Superior tensile properties of 1%C–CoCrFeMnNi high-entropy alloy additively manufactured by selective laser melting, *Mater. Res. Lett.*, **8**: 1–7 (2020); https://doi.org/10.1080/21663831.2019.1638844

18. F. Zhang, S. Zhao, K. Jin, H. Bei, and D. Popov, Pressure-induced fcc to hcp phase transition in Ni-based high entropy solid solution alloys, *Appl. Phys. Lett.*, **110**: 011902 (2017);
https://doi.org/DOI:101063/14973627
19. S. Mridha, M. Sadeghilaridjani, and S. Mukherjee, Activation volume and energy for dislocation nucleation in multi-principal element alloys, *Metals*, **9**, No. 2: 263 (2019);
https://doi.org/10.3390/met9020263
20. Y. Zhang, Y.J. Zhou, J.P. Lin, G.L. Chen, and P.K. Liaw, Solid-solution phase formation rules for multi-component alloys, *Adv. Eng. Mater.*, **10**: 534–538 (2008);
https://doi.org/10.1002/adem.200700240
21. C. Zhu, Z.P. Lu, and T.G. Nieh, Incipient plasticity and dislocation nucleation of FeCoCrNiMn high-entropy alloy, *Acta Mater.*, **61**: 2993–3001 (2013);
https://doi.org/10.1016/j.actamat.2013.01.059
22. Y. Brif, M. Thomas, and I. Todd, The use of high-entropy alloys in additive manufacturing, *Scr. Mater.*, **99**: 93–96 (2015);
https://doi.org/10.1016/j.scriptamat.2014.11.037
23. Y. Deng, C.C. Tasan, K.G. Pradeep, H. Springer, A. Kostka, and D. Raabe, Design of a twinning-induced plasticity high entropy alloy, *Acta Mater.*, **94**: 124–133 (2015).
https://doi.org/10.1016/j.actamat.2015.04.014
24. C. Li, J.C. Li, M. Zhao, and Q. Jiang, Effect of alloying elements on microstructure and properties of multiprincipal elements high-entropy alloys, *J. Alloys Compd.*, **475**: 752–757 (2009);
https://doi.org/10.1016/j.jallcom.2008.07.124
25. O.N. Senkov, J.M. Scott, S.V. Senkova, D.B. Miracle, and C.F. Woodward, Microstructure and room temperature properties of a high-entropy TaNbHfZrTi alloy, *J. Alloys Compd.*, **509**: 6043–6048 (2011);
https://doi.org/10.1016/j.jallcom.2011.02.171
26. N.N. Guo, L. Wang, L.S. Luo, X.Z. Li, Y.Q. Su, J.J. Guo, and H.Z. Fu, Microstructure and mechanical properties of refractory MoNbHfZrTi high-entropy alloy, *Mater. Des.*, **81**: 87–94 (2015);
https://doi.org/10.1016/j.matdes.2015.05.019
27. S. Maiti and W. Steurer, Structural-disorder and its effect on mechanical properties in single-phase TaNbHfZr high-entropy alloy, *Acta Mater.*, **106**: 87–97 (2016);
https://doi.org/10.1016/j.actamat.2016.01.018
28. M.C. Gao, B. Zhang, S.M. Guo, J.W. Qiao, and J.A. Hawk, High-entropy alloys in hexagonal close-packed structure, *Metall. Mater. Trans. A*, **47**: 3322 (2016);
https://doi.org/10.1007/s11661-015-3091-1
29. Z. Li, K.G. Pradeep, Y. Deng, D. Raabe, and C.C. Tasan, Metastable high-entropy dual-phase alloys overcome the strength–ductility trade-off, *Nature*, **534**: 227–230., (2016).
https://doi.org/10.1038/nature17981
30. J.M. Zhu, H. Fu, H. Zhang, A.M. Wang, H. Li, and Z. Hu, Microstructures and compressive properties of multicomponent AlCoCrFeNiMo x alloys, *Mater. Sci. Eng. A*, **527**: 6975–6979 (2010);
https://doi.org/10.1016/j.msea.2010.07.028
31. G. Laplanche, A. Kostka, O.M. Horst, G. Eggeler, and E.P. George, Microstructure evolution and critical stress for twinning in the CrMnFeCoNi high-entropy

alloy, *Acta Mater.*, **118**: 152–163 (2016);
https://doi.org/10.1016/j.actamat.2016.07.038
32. M.J. Jang, S.-H. Joo, C.-W. Tsai, J.-W. Yeh, and H. Kim, Compressive deformation behavior of CrMnFeCoNi high-entropy alloy, *Met. Mater. Int.*, **22**: 982–986 (2016);
https://doi.org/10.1007/s12540-016-6304-2
33. M. Chinababu, N. Naga Krishna, K. Sivaprasad, K.G. Prashanth, and E. Bhaskara Rao, Evolution of microstructure and mechanical properties of LM25–HEA composite processed through stir casting with a bottom pouring system, *Materials*, **15**: 230 (2022);
https://doi.org/10.3390/ma15010230
34. Q.H. Li, T.M. Yue, Z.N. Guo, and X. Lin, Microstructure and corrosion properties of AlCoCrFeNi high entropy alloy coatings deposited on AISI 1045 steel by the electrospark process, *Metall. Mater. Trans. A*, **44**: 1767–1778 (2013);
https://doi.org/10.1007/s11661-012-1535-4
35. N. Eißmann, B. Klöden, T. Weißgärber, and B. Kieback, High-entropy alloy CoCrFeMnNi produced by powder metallurgy, *Powder Metall.*, **60**: 184–197 (2017);
https://doi.org/10.1080/00325899.2017.1318480
36. Y. Wang, T. Voisin, J. McKeown, J. Ye, N. Calta, Z. Li, Z. Zeng, Y. Zhang, W. Chen, T. Roehling, R. Ott, M. Santala, P.J. Depond, M. Matthews, A. Hamza, and T. Zhu, Additively manufactured hierarchical stainless steels with high strength and ductility, *Nat. Mater.*, **17**: 63–71 (2018);
https://doi.org/10.1038/nmat5021
37. W. Xu, E.W. Lui, A. Pateras, M. Qian, and M. Brandt, In situ tailoring microstructure in additively manufactured Ti–6Al–4V for superior mechanical performance, *Acta Mater.*, **125**: 390–400 (2017);
https://doi.org/10.1016/j.actamat.2016.12.027
38. W. Xu, M. Brandt, S. Sun, J. Elambasseril, Q. Liu, K. Latham, K. Xia, and M. Qian, Additive manufacturing of strong and ductile Ti–6Al–4V by selective laser melting via in situ martensite decomposition, *Acta Mater.*, **85**: 74–84 (2015);
https://doi.org/10.1016/j.actamat.2014.11.028
39. R. Zhou, Y. Liu, B. Liu, L. Jia, and Q. Fang, Precipitation behavior of selective laser melted FeCoCrNiC 0.05 high entropy alloy, *Intermetallics*, **106**: 20–25 (2019);
https://doi.org/10.1016/j.intermet.2018.12.001
40. T. Fujieda, H. Shiratori, K. Kuwabara, M. Hirota, T. Kato, K. Yamanaka, Y. Koizumi, A. Chiba, and S. Watanabe, CoCrFeNiTi-based high-entropy alloy with superior tensile strength and corrosion resistance achieved by a combination of additive manufacturing using selective electron beam melting and solution treatment, *Mater. Lett.*, **189**: 148–151 (2017);
https://doi.org/10.1016/j.matlet.2016.11.026
41. X.H. An, X. Liao, Z.G. Zhu, B. Nguyen, F. Ng, P.K. Liaw, M.L.S. Nai, and J. Wei, Hierarchical microstructure and strengthening mechanisms of a CoCrFeNiMn high entropy alloy additively manufactured by selective laser melting, *Scr. Mater.*, **154**: 20–24 (2018);
https://doi.org/10.1016/j.scriptamat.2018.05.015
42. A. Piglione, B. Dovgyy, C. Liu, C.M. Gourlay, P.A. Hooper, and M.S. Pham, Printability and microstructure of the CoCrFeMnNi high-entropy alloy fabricated by laser powder bed fusion, *Mater. Lett.*, **224**: 22–25 (2018).
https://doi.org/10.1016/j.matlet.2018.04.052
43. W. Wu, R. Zhou, B. Wei, S. Ni, Y. Liu, and M. Song, Nanosized precipitates and dislocation networks reinforced C-containing CoCrFeNi high-entropy alloy

fabricated by selective laser melting, *Mater. Charact.*, **144**: 605–610 (2018); https://doi.org/DOI:101016/jmatchar201808019.
44. T. Borkar, V. Chaudhary, B. Gwalani, D. Choudhuri, C. V Mikler, V. Soni, T. Alam, R.V. Ramanujan, and R. Banerjee, A combinatorial approach for assessing the magnetic properties of high entropy alloys: role of Cr in $AlCo_xCr_{1-x}FeNi$, *Adv. Eng. Mater.*, **19**: 1700048 (2017); https://doi.org/10.1002/adem.201700048
45. B. Zheng, Y. Zhou, J.E. Smugeresky, J.M. Schoenung, and E. Lavernia, Thermal behavior and microstructural evolution during laser deposition with laser-engineered net shaping: Part I. Numerical calculations, *Metall. Mater. Trans. A*, **39**: 2228–2236 (2008); https://doi.org/10.1007/s11661-008-9557-7
46. Z. Sun, X. Tan, M. Descoins, D. Mangelinck, S. Tor, and C. Lim, Revealing hot tearing mechanism for an additively manufactured high-entropy alloy via selective laser melting, *Scr. Mater.*, **168**: 129–133 (2019); https://doi.org/10.1016/j.scriptamat.2019.04.036
47. C. Haase, F. Tang, M.B. Wilms, A. Weisheit, and B. Hallstedt, Combining thermodynamic modeling and 3D printing of elemental powder blends for high-throughput investigation of high-entropy alloys — Towards rapid alloy screening and design, *Mater. Sci. Eng. A*, **688**: 180–189 (2017); https://doi.org/10.1016/j.msea.2017.01.099
48. Z. Qiu, C. Yao, K. Feng, Z. Li, and P. Chu, Cryogenic deformation mechanism of CrMnFeCoNi high-entropy alloy fabricated by laser additive manufacturing process, *Int. J. Light. Mater. Manuf.*, **1**: 33–39 (2018); https://doi.org/10.1016/j.ijlmm.2018.02.001
49. Y. Chew, G. Bi, Z.G. Zhu, F. Ng, F. Weng, S. Liu, M.L.S. Nai, and B.Y. Lee, Microstructure and enhanced strength of laser aided additive manufactured CoCrFeNiMn high entropy alloy, *Mater. Sci. Eng. A*, **744**: 137–144 (2018); https://doi.org/10.1016/j.msea.2018.12.005
50. M. Moorehead, K. Bertsch, M. Niezgoda, C. Parkin, M. Elbakhshwan, K. Sridharan, C. Zhang, D. Thoma, and A. Couet, High-throughput synthesis of Mo–Nb–Ta–W high-entropy alloys via additive manufacturing, *Mater. Des.*, **187**: 108358 (2020); https://doi.org/10.1016/j.matdes.2019.108358
51. H. Dobbelstein, E.L. Gurevich, E.P. George, A. Ostendorf, and G. Laplanche, Laser metal deposition of compositionally graded TiZrNbTa refractory high-entropy alloys using elemental powder blends, *Addit. Manuf.*, **25**: 252–262 (2019); https://doi.org/10.1016/j.addma.2018.10.042
52. I. Kunce, M. Polanski, and J. Bystrzycki, Structure and hydrogen storage properties of a high entropy ZrTiVCrFeNi alloy synthesized using Laser Engineered Net Shaping (LENS), *Int. J. Hydrogen Energy*, **38**: 12180–12189 (2013); https://doi.org/10.1016/j.ijhydene.2013.05.071
53. P.K. Sarswat, S. Sarkar, A. Murali, W. Huang, W. Tan, and M.L. Free, Additive manufactured new hybrid high entropy alloys derived from the AlCoFeNiSm-TiVZr system, *Appl. Surf. Sci.*, **476**: 242–258 (2019); https://doi.org/10.1016/j.apsusc.2018.12.300
54. L. Ladani and M. Sadeghilaridjani, Review of powder bed fusion additive manufacturing for metals, *Metals*, **11**: 1391 (2021); https://doi.org/10.3390/met11091391
55. M. Sadeghilaridjani, S. Muskeri, V. Hasannaeimi, M. Pole, and S. Mukherjee, Strain rate sensitivity of a novel refractory high entropy alloy: Intrinsic versus

extrinsic effects, *Mater. Sci. Eng. A*, **766**: 138326 (2019); https://doi.org/10.1016/j.msea.2019.138326
56. P.J. Barron, A.W. Carruthers, J.W. Fellowes, N.G. Jones, H. Dawson, and E.J. Pickering, Towards V-based high-entropy alloys for nuclear fusion applications, *Scr. Mater.*, **176**: 12–16 (2020); https://doi.org/10.1016/j.scriptamat.2019.09.028
57. T. Yang, Y.L. Zhao, J.H. Luan, B. Han, J. Wei, J.J. Kai, and C.T. Liu, Nanoparticles-strengthened high-entropy alloys for cryogenic applications showing an exceptional strength-ductility synergy, *Scr. Mater.*, **164**: 30–35 (2019); https://doi.org/10.1016/j.scriptamat.2019.01.034
58. T. Fujieda, H. Shiratori, K. Kuwabara, T. Kato, K. Yamanaka, Y. Koizumi, and A. Chiba, First demonstration of promising selective electron beam melting method for utilizing high-entropy alloys as engineering materials, *Mater. Lett.*, **159**: 12–15 (2015); https://doi.org/10.1016/j.matlet.2015.06.046
59. K. Kuwabara, H. Shiratori, T. Fujieda, K. Yamanaka, Y. Koizumi, and A. Chiba, Mechanical and corrosion properties of AlCoCrFeNi high-entropy alloy fabricated with selective electron beam melting, *Addit. Manuf.*, **23**: 264–271 (2018); https://doi.org/10.1016/j.addma.2018.06.006
60. H. Shiratori, T. Fujieda, K. Yamanaka, Y. Koizumi, K. Kuwabara, T. Kato, and A. Chiba, Relationship between the microstructure and mechanical properties of an equiatomic AlCoCrFeNi high-entropy alloy fabricated by selective electron beam melting, *Mater. Sci. Eng. A*, **656**: 39–46 (2016); https://doi.org/10.1016/j.msea.2016.01.019
61. P. Wang, P. Huang, F.L. Ng, W.J. Sin, S. Lu, M.L.S. Nai, Z. Dong, and J. Wei, Additively manufactured CoCrFeNiMn high-entropy alloy via pre-alloyed powder, *Mater. Des.*, **168**: 107576 (2019). https://doi.org/10.1016/j.matdes.2018.107576
62. P.D. Niu, R.D. Li, T.C. Yuan, S.Y. Zhu, C. Chen, M.B. Wang, and L. Huang, Microstructures and properties of an equimolar AlCoCrFeNi high entropy alloy printed by selective laser melting, *Intermetallics.*, **104**: 24–32 (2019); https://doi.org/10.1016/j.intermet.2018.10.018
63. S. Luo, C. Zhao, Y. Su, Q. Liu, and Z. Wang, Selective laser melting of dual phase AlCrCuFeNix high entropy alloys: Formability, heterogeneous microstructures and deformation mechanisms, *Addit. Manuf.*, **31**: 100925 (2020); https://doi.org/10.1016/j.addma.2019.100925
64. D. Lin, L. Xu, H. Jing, Y. Han, L. Zhao, and F. Minami, Effects of annealing on the structure and mechanical properties of FeCoCrNi high-entropy alloy fabricated via selective laser melting, *Addit. Manuf.*, **32**: 101058 (2020). https://doi.org/10.1016/j.addma.2020.101058
65. R. Li, P. Niu, T. Yuan, P. Cao, C. Chen, and K. Zhou, Selective laser melting of an equiatomic CoCrFeMnNi high-entropy alloy: Processability, non-equilibrium microstructure and mechanical property, *J. Alloys Compd.*, **746**: 125–134 (2018); https://doi.org/10.1016/j.jallcom.2018.02.298
66. Z. Tong, X. Ren, J. Jiao, W. Zhou, Y. Ren, Y. Ye, E.A. Larson, and J. Gu, Laser additive manufacturing of FeCrCoMnNi high-entropy alloy: Effect of heat treatment on microstructure, residual stress and mechanical property, *J. Alloys Compd.*, **785**: 1144–1159 (2019); https://doi.org/10.1016/j.jallcom.2019.01.213
67. Z. Xu, H. Zhang, X. Du, Y. He, H. Luo, G. Song, L. Mao, T. Zhou, and L. Wang, Corrosion resistance enhancement of CoCrFeMnNi high-entropy alloy fabricated

by additive manufacturing, *Corros. Sci.*, **177**: 108954 (2020); https://doi.org/10.1016/j.corsci.2020.108954
68. Z. Xu, H. Zhang, W. Li, A. Mao, L. Wang, G. Song, and Y. He, Microstructure and nanoindentation creep behavior of CoCrFeMnNi high-entropy alloy fabricated by selective laser melting, *Addit. Manuf.*, **28**: 766–771 (2019); https://doi.org/10.1016/j.addma.2019.06.012
69. A. Ostovari Moghaddam, N.A. Shaburova, M.N. Samodurova, A. Abdollahzadeh, and E.A. Trofimov, Additive manufacturing of high entropy alloys: A practical review, *J. Mater. Sci. Technol.*, **77**: 131–162 (2021). https://doi.org/10.1016/j.jmst.2020.11.029
70. Z. Zhu, X.H. An, W. Lu, Z. Li, F. Ng, X. Liao, U. Ramamurty, M.L.S. Nai, and J. Wei, Selective laser melting enabling the hierarchically heterogeneous microstructure and excellent mechanical properties in an interstitial solute strengthened high entropy alloy, *Mater. Res. Lett.*, **7**: 453–459 (2019); https://doi.org/10.1080/21663831.2019.1650131
71. Z. Li, C.C. Tasan, H. Springer, B. Gault, and D. Raabe, Interstitial atoms enable joint twinning and transformation induced plasticity in strong and ductile high-entropy alloys, *Sci. Rep.*, **7**: 40704 (2017); https://doi.org/10.1038/srep40704
72. M.R.U. Ahsan, G.-J. Seo, X. Fan, P.K. Liaw, S. Motaman, C. Haase, and D.B. Kim, Effects of process parameters on bead shape, microstructure, and mechanical properties in wire + arc additive manufacturing of $Al_{0.1}$CoCrFeNi high-entropy alloy, *J. Manuf. Process.*, **68**: 1314–1327 (2021); https://doi.org/10.1016/j.jmapro.2021.06.047
73. Q. Shen, X. Kong, and X. Chen, Fabrication of bulk Al–Co–Cr–Fe–Ni high-entropy alloy using combined cable wire arc additive manufacturing (CCW-AAM): Microstructure and mechanical properties, *J. Mater. Sci. Technol.*, **74**: 136–142 (2021); https://doi.org/10.1016/j.jmst.2020.10.037
74. A. Zavdoveev, A. Klapatyuk, T. Baudin, E. MacDonald, D. Mohan, J. Oliveira, A. Gajvoronskiy, V. Poznyakov, H.S. Kim, F. Brisset, M. Khokhlov, M. Heaton, M. Rogante, M. Skoryk, D. Vedel, R. Kozin, I. Klochkov, and S. Motrunich, Non-equimolar Cantor high entropy alloy fabrication using metal powder cored wire arc additive manufacturing, *Addit. Manuf. Lett.*, **6**: 100124 (2023); https://doi.org/10.1016/j.addlet.2023.100124
75. A. Zavdoveev, T. Baudin, E. Pashinska, H.S. Kim, F. Brisset, M. Heaton, V. Poznyakov, M. Rogante, V. Tkachenko, I. Klochkov, and M. Skoryk, Continuous severe plastic deformation of low-carbon steel: physical–mechanical properties and multiscale structure analysis, *Steel Res. Int.*, **92**: 2000482 (2021); https://doi.org/10.1002/srin.202000482
76. N.H. Sateesh, G.C.M. Kumar, K. Prasad, S. C.K., and A.R. Vinod, Microstructure and mechanical characterization of laser sintered inconel-625 superalloy, *Procedia Mater. Sci.*, **5**: 772–779 (2014); https://doi.org/10.1016/j.mspro.2014.07.327
77. Q. Jia and D. Gu, Selective laser melting additive manufacturing of Inconel 718 superalloy parts: Densification, microstructure and properties, *J. Alloys Compd.*, **585**: 713–721 (2014); https://doi.org/10.1016/j.jallcom.2013.09.171
78. J.A. Muciz-Lerma, A. Nommeots-Nomm, K.E. Waters, and M. Brochu, A comprehensive approach to powder feedstock characterization for powder bed fusion additive manufacturing: a case study on $AlSi_7Mg$, *Mater.*, **11**: 2386 (2018); https://doi.org/10.3390/ma11122386

79. X. Zhao, J. Chen, X. Lin, and W. Huang, Study on microstructure and mechanical properties of laser rapid forming Inconel 718, *Mater. Sci. Eng. A*, **478**: 119–124 (2008);
https://doi.org/10.1016/j.msea.2007.05.079
80. A.H. Nickel, D.M. Barnett, and F.B. Prinz, Thermal stresses and deposition patterns in layered manufacturing, *Mater. Sci. Eng. A*, **317**: 59–64 (2001);
https://doi.org/10.1016/S0921-5093(01)01179-0
81. L. Wang, N. Wang, W.J. Yao, and Y. Zheng, Effect of substrate orientation on the columnar-to-equiaxed transition in laser surface remelted single crystal superalloys, *Acta Mater.*, **88**: 283–292(2015);
https://doi.org/10.1016/j.actamat.2015.01.063
82. D. Gu and Y. Shen, Balling phenomena in direct laser sintering of stainless steel powder: Metallurgical mechanisms and control methods, *Mater. Des.*, **30**: 2903–2910 (2009);
https://doi.org/10.1016/j.matdes.2009.01.013
83. D.B. Hann, J. Iammi, and J. Folkes, A simple methodology for predicting laser-weld properties from material and laser parameters, *J. Phys. D: Appl. Phys.*, **44**: 445401 (2011).
https://doi.org/10.1088/0022-3727/44/44/445401
84. T. Vilaro, C. Colin, J.D. Bartout, L. Nazé, and M. Sennour, Microstructural and mechanical approaches of the selective laser melting process applied to a nickel-base superalloy, *Mater. Sci. Eng. A*, **534**: 446–451 (2012);
https://doi.org/10.1016/j.msea.2011.11.092
85. K.G. Prashanth, S. Scudino, H.J. Klauss, K.B. Surreddi, L. Löber, Z. Wang, A.K. Chaubey, U. Kühn, and J. Eckert, Microstructure and mechanical properties of Al–12Si produced by selective laser melting: Effect of heat treatment, *Mater. Sci. Eng. A*, **590**: 153–160 (2014);
https://doi.org/10.1016/j.msea.2013.10.023
86. W. Wu, J. Jiang, H. Jiang, W. Liu, G. Li, B. Wang, M. Tang, and J. Zhao, Improving bending and dynamic mechanics performance of 3D printing through ultrasonic strengthening, *Mater. Lett.*, **220**: 317–320 (2018).
https://doi.org/10.1016/j.matlet.2018.03.048
87. Q.H. Tang, Y. Huang, Y.Y. Huang, X.Z. Liao, T.G. Langdon, and P.Q. Dai, Hardening of an $Al_{0.3}$CoCrFeNi high entropy alloy via high-pressure torsion and thermal annealing, *Mater. Lett.*, **151**: 126–129 (2015);
https://doi.org/10.1016/j.matlet.2015.03.066
88. A. V Kuznetsov, D.G. Shaysultanov, N.D. Stepanov, G.A. Salishchev, and O.N. Senkov, Tensile properties of an AlCrCuNiFeCo high-entropy alloy in as-cast and wrought conditions, *Mater. Sci. Eng. A*, **533**: 107–118 (2012);
https://doi.org/10.1016/j.msea.2011.11.045.
89. C.-W. Tsai, Y.-L. Chen, M.-H. Tsai, J.-W. Yeh, T.-T. Shun, and S.-K. Chen, Deformation and annealing behaviors of high-entropy alloy $Al_{0.5}$CoCrCuFeNi, *J. Alloys Compd.*, **486**: 427–435 (2009);
https://doi.org/10.1016/j.jallcom.2009.06.182
90. Y.-F. Kao, T.-J. Chen, S.-K. Chen, and J.-W. Yeh, Microstructure and mechanical property of as-cast, -homogenized, and -deformed Al_xCoCrFeNi ($0 \le x \le 2$) high-entropy alloys, *J. Alloys Compd.*, **488**: 57–64 (2009);
https://doi.org/10.1016/j.jallcom.2009.08.090
91. T.-T. Shun and Y.-C. Du, Age hardening of the $Al_{0.3}CoCrFeNiC_{0.1}$ high entropy alloy, *J. Alloys Compd.*, **478**: 269–272 (2009);
https://doi.org/10.1016/j.jallcom.2008.12.014

92. J. Joseph, P. Hodgson, T. Jarvis, X. Wu, N. Stanford, and D.M. Fabijanic, Effect of hot isostatic pressing on the microstructure and mechanical properties of additive manufactured Al_xCoCrFeNi high entropy alloys, *Mater. Sci. Eng. A*, **733**: 59–70 (2018);
https://doi.org/10.1016/j.msea.2018.07.036
93. X. Zhao, X. Lin, J. Chen, L. Xue, and W. Huang, The effect of hot isostatic pressing on crack healing, microstructure, mechanical properties of Rene88DT superalloy prepared by laser solid forming, *Mater. Sci. Eng. A*, **504**: 129–134 (2009).
https://doi.org/10.1016/j.msea.2008.12.024
94. M.T. Kim, S.Y. Chang, and J.B. Won, Effect of HIP process on the microstructural evolution of a nickel-based superalloy, *Mater. Sci. Eng. A*, **441**: 126–134 (2006);
https://doi.org/10.1016/j.msea.2006.09.060
95. C.-M. Lin and H.-L. Tsai, Effect of annealing treatment on microstructure and properties of high-entropy $FeCoNiCrCu_{0.5}$ alloy, *Mater. Chem. Phys.*, **128**: 50–56 (2011).
https://doi.org/10.1016/j.matchemphys.2011.02.022
96. N.D. Stepanov, D.G. Shaysultanov, N.Y. Yurchenko, S.V. Zherebtsov, A.N. Ladygin, G.A. Salishchev, and M.A. Tikhonovsky, High temperature deformation behavior and dynamic recrystallization in CoCrFeNiMn high entropy alloy, *Mater. Sci. Eng. A*, **636**: 188–195 (2015);
https://doi.org/10.1016/j.msea.2015.03.097
97. Y. Geng, S.V. Konovalov, and X. Chen, Research status and application of the high-entropy and traditional alloys fabricated via the laser cladding, *Prog. Phys. Met.*, **21**, No. 1: 26–45 (2020);
https://doi.org/10.15407/ufm.21.01.026
98. M.O. Vasylyev, B.M. Mordyuk, and S.M. Voloshko, Wire-feeding based additive manufacturing of the Ti–6Al–4V Alloy. Part I. Microstructure, *Prog. Phys. Met.*, **24**, No. 1: 5–37 (2023);
https://doi.org/10.15407/ufm.24.01.005
99. M.O. Vasylyev, B.M. Mordyuk, and S.M. Voloshko, Wire-feeding based additive manufacturing of the Ti–6Al–4V Alloy. Part II. Mechanical properties, *Prog. Phys. Met.*, **24**, No. 1: 38–74 (2023);
https://doi.org/10.15407/ufm.24.01.038
100. O.M. Ivasishin, D.V. Kovalchuk, P.E. Markovsky, D.G. Savvakin, O.O. Stasiuk, V.I. Bondarchuk, D.V. Oryshych, S.G. Sedov, and V.A. Golub, Additive manufacturing of titanium-based materials using electron beam wire 3*D* printing approach: peculiarities, advantages, and prospects, *Prog. Phys. Met.*, **24**, No. 1: 75–105 (2023);
https://doi.org/10.15407/ufm.24.01.075

Received 31.05.2023;
in final version, 18.07.2023

А.В. Завдовєєв[1], *Т. Баудін*[2], *Д.Г. Моган*[3],
Д.Л. Пакула[4], *Д.В. Ведель*[5], *М.А. Скорик*[4]

[1] Інститут електрозварювання ім. Є.О. Патона НАН України,
вул. Казимира Малевича, 11, 03150 Київ, Україна

[2] Університет Париж-Сакле, НЦНД,
Інститут молекулярної хімії та матеріалів Орсе,
91405 Орсе, Франція

[3] Кафедра технології оброблення матеріялів,
Науково-дослідний інститут Чженчжоу Харбінського технологічного інституту,
Чженчжоу, Китай

[4] Інститут металофізики ім. Г.В. Курдюмова НАН України,
бульв. Академіка Вернадського, 36, 03142 Київ, Україна

[5] Інститут проблем матеріалознавства ім. І.М. Францевича НАН України,
вул. Омеляна Пріцака, 3, 03142 Київ, Україна

ОСНОВИ ПРОЦЕСІВ АДИТИВНОГО ВИРОБНИЦТВА ВИСОКОЕНТРОПІЙНИХ СТОПІВ

В огляді запропоновано комплексний аналіз процесів адитивного виробництва (АВ) у застосуванні до високоентропійних стопів (ВЕС). В останні роки ВЕС привернули значну увагу завдяки своїм унікальним механічним і фізичним властивостям. Надано історичну довідку та чітке визначення ВЕС з описом розвитку їх з часом. Основну увагу зосереджено на вивченні використання процесів АВ у ВЕС. Зокрема, обговорено три відомі методи АВ: електронно-променеві процеси, оброблені лазером ВЕС та дугове адитивне виробництво. Кожен метод детально досліджено, включаючи його переваги, обмеження та поточні застосування в галузі ВЕС. Акцентовано увагу на важливості параметрів процесу АВ під час виготовлення ВЕС. Проаналізовано такі параметри як потужність лазера, швидкість сканування та швидкість подачі порошку задля впливу їх на мікроструктуру та механічні властивості кінцевого продукту. Розглянуто методи пост-оброблення для ВЕС, виготовлених за допомогою добавок. Підкреслено важливість таких етапів як термічне оброблення, фінішне оброблення поверхні та механічне оброблення для досягнення бажаних властивостей матеріалу та точности розмірів у компонентів ВЕС, виготовлених АВ. З оглядом ВЕС, застосування їх у процесах АВ, впливу параметрів процесу та міркувань щодо пост-оброблення ця робота може слугувати корисним джерелом інформації для дослідників на шляху до поліпшення розуміння та впровадження АВ у ВЕС.

Ключові слова: адитивне виробництво, високоентропійні стопи, оброблення, структура, властивості.